4450–4463 *Nucleic Acids Research, 2011, Vol. 39, No. 10* *Published online 28 January 2011*
doi:10.1093/nar/gkr025

Mapping interactions between the RNA chaperone FinO and its RNA targets

David C. Arthur[1], Ross A. Edwards[1], Susan Tsutakawa[2], John A. Tainer[2,3], Laura S. Frost[4] and J. N. Mark Glover[1,*]

[1]Department of Biochemistry, University of Alberta, Edmonton, AB T6G 2H7, Canada, [2]Life Sciences Division, Department of Genome Stability, Lawrence Berkeley National Laboratory, Berkeley, CA 94720, [3]Department of Molecular Biology and The Skaggs Institute for Chemical Biology, The Scripps Research Institute, 10550 North Torrey Pines Road, MB4, La Jolla, CA 92037, USA and [4]Department of Biological Sciences, University of Alberta, Edmonton, AB T6G 2E9, Canada

Received August 11, 2010; Revised January 10, 2011; Accepted January 12, 2011

ABSTRACT

Bacterial conjugation is regulated by two-component repression comprising the antisense RNA FinP, and its protein co-factor FinO. FinO mediates base-pairing of FinP to the 5′-untranslated region (UTR) of *traJ* mRNA, which leads to translational inhibition of the transcriptional activator TraJ and subsequent down regulation of conjugation genes. Yet, little is known about how FinO binds to its RNA targets or how this interaction facilitates FinP and *traJ* mRNA pairing. Here, we use solution methods to determine how FinO binds specifically to its minimal high affinity target, FinP stem–loop II (SLII), and its complement SLIIc from *traJ* mRNA. Ribonuclease footprinting reveals that FinO contacts the base of the stem and the 3′ single-stranded tails of these RNAs. The phosphorylation or oxidation of the 3′-nucleotide blocks FinO binding, suggesting FinO binds the 3′-hydroxyl of its RNA targets. The collective results allow the generation of an energy-minimized model of the FinO–SLII complex, consistent with small-angle X-ray scattering data. The repression complex model was constrained using previously reported cross-linking data and newly developed footprinting results. Together, these data lead us to propose a model of how FinO mediates FinP/*traJ* mRNA pairing to down regulate bacterial conjugation.

INTRODUCTION

Plasmid conjugation is a major mechanism of horizontal gene transfer between bacteria, and is responsible for the rapid spread of virulence and antibiotic resistance factors throughout bacterial populations. The study of the conjugative transfer of F and F-like plasmids in *Escherichia coli* has provided important insights into the mechanisms underlying this process (1,2). Cells newly infected with many of the plasmids from the F family are initially competent to express the major plasmid transcriptional unit, the *tra* operon, and efficiently transfer plasmid to recipient cells. Gradually, however, *tra* expression is repressed, and conjugation is attenuated. The initial burst of conjugation spreads the plasmid throughout a population. The subsequent repression of the conjugation machinery likely protects the plasmid-bearing cells from infection by pili-specific bacteriophage, and reduces the metabolic burden of plasmid maintenance.

Repression of conjugation relies on a plasmid-encoded antisense RNA system called FinOP. The antisense RNA, FinP, is complementary to the 5′-UTR of *traJ*, the transcriptional activator of the *tra* operon (3–6) (Figure 1A and B). Binding of FinP to the *traJ* mRNA occludes the ribosomal binding site, inhibiting *traJ* translation and preventing *tra* operon expression via H-NS de-silencing (7). FinP alone, however, is unable to repress conjugation, in part because it is rapidly degraded by RNaseE, a component of the *E. coli* RNA degradosome (8,9). FinP requires a second plasmid factor, the FinO protein, which binds FinP and stabilizes it against degradation (8,10). FinO also binds the *traJ* 5′-UTR, and facilitates FinP–*traJ*

*To whom correspondence should be addressed. Tel: +1 780 492 2136; Fax: +1 780 492 0886; Email: mark.glover@ualberta.ca
Correspondence may also be addressed to Ross A. Edwards. Tel: +1 780 492 4575; Fax: +1 780 492 0886; Email: ross.edwards@ualberta.ca

The authors wish it to be known that, in their opinion, the first two authors should be regarded as joint First Authors.

RNA interactions, to ultimately repress conjugation 100- to 1000-fold.

FinO recognizes multiple stem–loop structures in both the FinP and *traJ* 5′-UTR RNAs, binding with highest affinity to FinP SLII (11). Stem–loop recognition is independent of the precise RNA sequence, but requires 5′ and 3′single-stranded tails adjacent to the duplex stem. The FinO protein adopts a novel protein fold with an extended α-helix and an unstructured N-terminal region (12) (Figure 1D). The C-terminal globular domain, $FinO_{45–186}$, which lacks the unstructured region and much of the extended α-helix, comprises the core RNA binding domain (12,13). Site-specific protein–RNA cross-linking studies have indicated that residues on one face of the globular domain, as well as near the N-terminal tip of the extended α-helix, contact SLII (14).

Perhaps the most intriguing aspect of FinO function is its ability to facilitate FinP–*traJ* RNA pairing (10,15,16). In spite of the perfect complementarities of these RNAs, duplexing is extremely slow in the absence of FinO because of the significant energy barriers posed by the highly stable internal stem–loops present in both RNAs. FinO not only facilitates duplexing, but also promotes strand exchange between a minimal SLII-like duplex substrate and a complementary single strand (15). This suggests that FinO may act by destabilizing the internal duplex structure, thereby lowering the free-energy barrier to intermolecular base-pairing interactions. Deletion analyses reveal that this activity requires the N-terminal disordered region as well as the N-terminus of the extended helix. A solvent-exposed tryptophan residue at the tip of the exposed N-terminal helix (Trp36) appears to be the most critical single residue for both RNA duplexing and strand exchange activities (15).

In this article, we used solution techniques to develop a structural model for the interaction between FinO and minimal, high-affinity target RNAs. Ribonuclease footprinting reveals that wild-type FinO and the truncation mutants, $FinO_{33–186}$ W36A and $FinO_{45–186}$, all contact FinP SLII and *traJ* SLIIc RNAs in a similar manner involving the base of the duplex stem and the 3′ single-stranded tail. FinO binding is blocked by phosphorylation of the 3′-end of the RNA, or oxidation of the 3′-ribose, suggesting a free 3′-hydroxyl group is essential for FinO binding. A complex of $FinO_{45–186}$ with SLII was modeled by docking the semi-flexible protein and RNA structures in an automated, energy-minimizing procedure employing distance restraints defined directly from our biochemical data. The model compared favorably with small-angle X-ray solution scattering data of the same complex. These data and the structural model were used to explore the relationship between FinO binding and its RNA chaperone activity.

MATERIALS AND METHODS

Cloning of FinO constructs

FinO constructs were cloned using Gateway Technology (Invitrogen) and the overlap extension PCR technique to introduce mutations (17). Forward *att*B PCR primers (Integrated DNA technologies) were designed to have the necessary homologous recombination sites and a cleavage site for Prescission protease (GE Healthcare). The sequences for the forward primers are: FinO WT Fwd (5′-GGG GAC AAG TTT GTA CAA AAA AGC AGG CTT CCT GGA AGT TCT GTT CCA GGG GCC CAT GAC AGA GCA GAA ACG ACC GGT A-3′), FinO 33W36A Fwd (5′-GGG GAC AAG TTT GTA CAA AAA AGC AGG CTT CCT GGA AGT TCT GTT CCA GGG GCC CCC ACC AAA AGC GAA GGT GAA A-3′), FinO 45 Fwd (5′-GGG GAC AAG TTT GTA CAA AAA AGC AGG CTT CCT GGA AGT TCT GTT CCA GGG GCC CGA GAA GGC TGC CCG GGA AGC AGA G-3′). The sequence for the reverse primer is: FinO 186 Rev (5′-GGG GAC CAC TTT GTA CAA GAA AGC TGG GTC CTA TCA TTG TTC ATC AAG CAC GGC CTG AAG TTC-3′). The primers were used to PCR off a pGEX-KG plasmid containing the FinO 1–186 gene (13). The amplified inserts were recombined into pDONR 201 and transferred to the pDEST-15 expression plasmid containing the glutathione-S-transferase gene. The sequence of the expression clones were verified for the correct FinO sequence by DNA sequencing (Molecular Biology Services Unit, University of Alberta Department of Biological Sciences).

Expression and purification of FinO constructs

Expression of each FinO-GST construct was described previously (13). Gel filtration chromatography was used to further purify the FinO constructs. Fractions containing FinO were concentrated and loaded onto a Superdex 75 26/60 gel-filtration column (GE Healthcare) which was equilibrated in 50 mM HEPES pH 7, 200 mM NaCl, 1 mM EDTA, 5 mM Tris(2-carboxyethyl) phosphine hydrochloride (TCEP) (Sigma-Aldrich). Purified FinO was concentrated to the desired concentration and protein concentrations were calculated using extinction coefficients at 280 nm determined experimentally by amino acid analysis (Alberta Peptide Institute): $FinO_{1–186}$ WT ($27\,872\ M^{-1}cm^{-1}$), $FinO_{33–186}$ W36A ($21\,263\ M^{-1}cm^{-1}$) and $FinO_{45–186}$ ($20\,469\ M^{-1}cm^{-1}$).

Preparation and labeling of RNA constructs for electrophoretic mobility shift and RNase footprinting experiments

SLII and SLIIc constructs (sequences shown in bold in Figure 1B and A) were chemically synthesized using an Applied Biosystems DNA synthesizer which was modified for RNA synthesis using Dharmacon 2′ ACE chemistry (18). The 5′-end-labeled RNAs were labeled with γ^{32}P-ATP (6000 Ci/mmol, Perkin Elmer) and T4 polynucleotide kinase (New England Biolabs). The 3′-end-labeled RNAs were labeled with 3′,5′-cytidine [5′-^{32}P] diphosphate (pCp) (Perkin Elmer) and T4 RNA Ligase I (New England Biolabs). Both labeling reactions were purified using denaturing gel electrophoresis. The 5′-end-labeled pellets were resuspended in 1 × TE pH 7.5, 10 mM NaCl. The 3′-end-labeled pellets were resuspended in 50 µl of ddH_2O. An additional T4 kinase

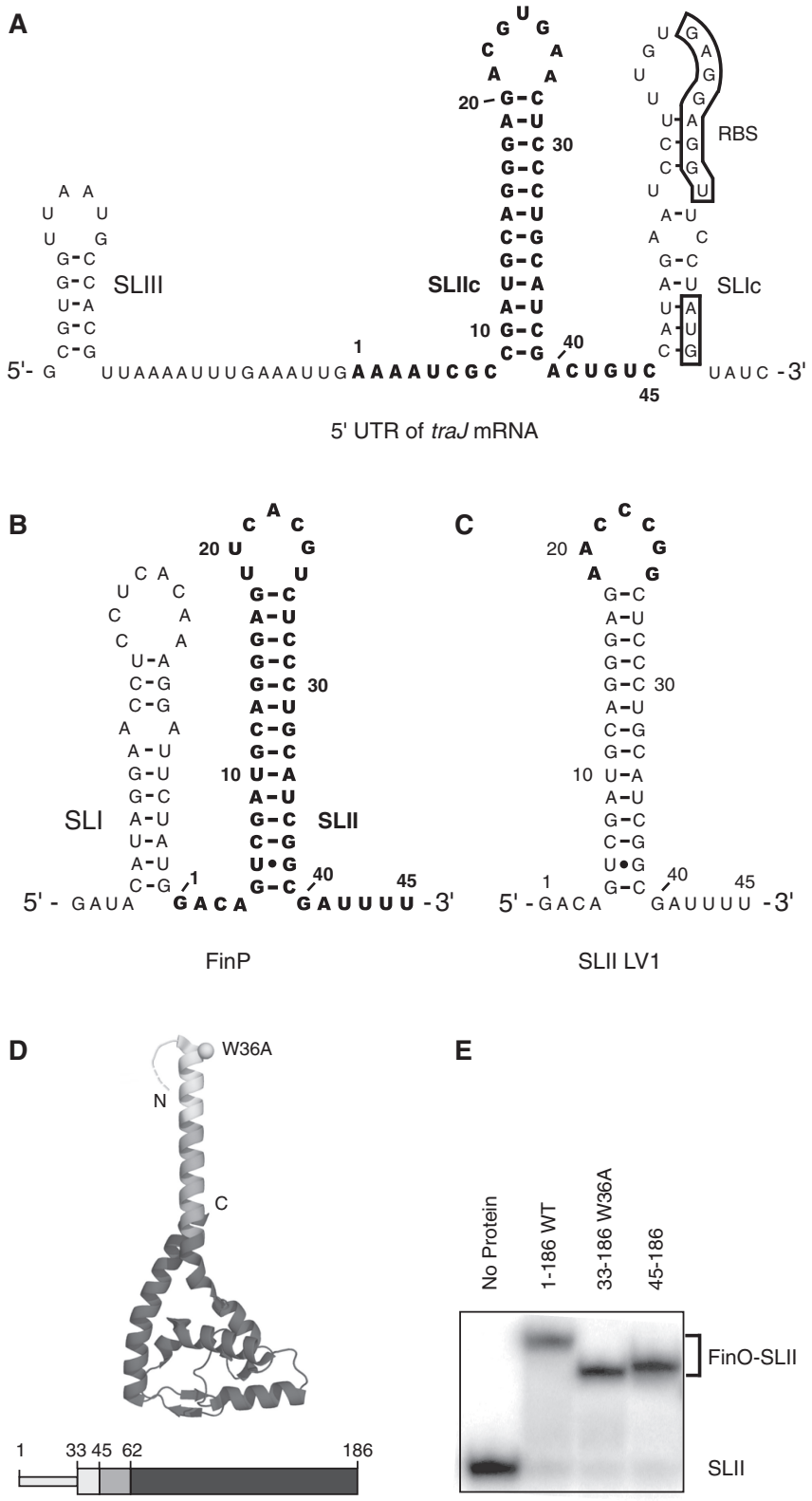

Figure 1. Overview of constructs used in the study. (**A** and **B**) The secondary structures of *traJ* mRNA and FinP, respectively. The ribosomal binding site and start codon of *traJ* mRNA are boxed. The derivative RNAs of focus, SLIIc and SLII, are shown in bold and numbered accordingly. (**C**) The secondary structure SLII LV1 RNA, used to form a complex with the $FinO_{45–186}$ in the SAXS experiments. SLII LV1 deviates from wild-type SLII in its loop region, which is shown in bold. (**D**) The crystal structure of $FinO_{26–186}$ highlighting the protein constructs used in the experiments. The W36A mutation is shown as a ball on the structure. The N-terminal 32 amino acids were not observed due to disorder in the structure and are drawn in (dashed section). Below is a scaled linear representation of the primary structure of FinO showing where each construct begins. The shades of gray correspond to the crystal structure coloring. (**E**) A representative 8% native PAGE demonstrating each of the FinO constructs in a 1:1 molar complex with 5′-^{32}P-SLII.

dephosphorylation step was needed to remove the 3′-phosphate from the added cytidine of the 3′-end-labeled RNAs which prevented binding of the FinO constructs. The 3′-dephosphorylated end-labeled RNAs were resuspended in 1 × TE pH 7.5, 10 mM NaCl. RNAs containing a 2′,3′ dialdehyde terminal ribose were generated by treatment of the 3′ dephosphorylated RNA with 10 mM $NaIO_4$. For each periodate reaction, 1 µl of dephosphorylated, annealed, ^{32}P-SLII was added to 99 µl of 10 mM $NaIO_4$. The reactions were incubated at 4°C for 40 min in the dark followed by ethanol precipitation. The pellets were washed and resuspended in 7 µl ddH_2O. The periodate-treated ^{32}P-SLII resuspensions were then added to 1 µl 10 × structure buffer (500 mM Tris–HCl pH 7.5, 1M NaCl, 100 mM $MgCl_2$), 1 µl of 2 mg/ml tRNA, and 1 µl 10 µM FinO (wild-type, 33-186 W36A or 45-186) or 1× structure buffer for the no protein reaction. Parallel binding reactions were performed for untreated, annealed, dephosphorylated ^{32}P-SLII RNA using 1 µl RNA, 1 µl 10× structure buffer, 1 µl of 2 mg/ml tRNA, 1 µl 10 µM FinO (wild-type, 33–186 W36A, or 45–186) or 1× structure buffer for the no protein reaction, and 7 µl ddH_2O. All 10 µl binding reactions were incubated at 4°C for 30 min before adding 10 µl of 20% glycerol and loading onto an 8% native polyacrylamide gel, equilibrated with 1× tris–glycine, pH 8.0 at 4°C. Prior to use in the footprinting experiments, all labeled RNA stocks were annealed by heating to 95°C for 1 min followed by slow cooling to room temperature. Electrophoretic mobility shift experiments were carried out as described previously (15).

RNase footprinting

Native electrophoretic mobility shift assays were used to find 1:1 molar ratio FinO–RNA complexes prior to footprinting experiments. The binding reactions for the RNase footprinting experiments were performed in 14 µl reactions: 1.5 µl of 10× structure buffer (500 mM Tris–HCl pH 7.5, 1 M NaCl, 100 mM $MgCl_2$), 1.5 µl of purified, annealed 5′ or 3′-^{32}P-SLII or SLIIc (in 10 mM Tris–HCl pH 7.5, 10 mM NaCl, 1 mM EDTA), 1.5 µl of protein sample (at 10× final concentration in 50 mM HEPES pH 7, 200 mM NaCl, 1 mM EDTA, 5 mM TCEP), 1.5 µl of 2 µg/µL tRNA (Ambion), and 8 µl ddH_2O. Reactions were incubated on ice for 30 min and aliquots of 5 µl of the reaction was removed and added to 5 µl of 20% glycerol and loaded onto an 8% native gel to assay binding. One microliter of RNase V1 or I (at the appropriate concentration; see below) was added to the remaining 9 µl of the binding reaction. RNase cleavage experiments were incubated at 4°C for 1 h and stopped immediately with 120 µl of 0.3 M NaOAc pH 5.3 and 130 µ l of phenol/chloroform/IAA. Samples were then chloroform extracted and ethanol precipitated. Pellets were resuspended in 4 µL of formamide gel load buffer and loaded on a 15% urea-denaturing sequencing gel. Gels were exposed overnight and quantitated using ImageQuant software (GE Healthcare). To determine the optimal amount of RNase V1 or I to add for the footprinting assays, we performed cleavage assays with end-labeled SLII or SLIIc (at the same concentration as the footprinting experiments) where the concentration of RNase V1 or I was increased until non-specific cleavages resulted. The reactions were incubated at the same temperature and length of time as the footprinting experiments. A final RNase V1 concentration of 0.001 U/µl and RNase I concentration of 0.01 U/µl gave specific cleavages with an adequate signal to noise.

We used two different methods to assign the RNase V1 cleavage products which, due to a 3′-OH, run slower on a denaturing gel. First, for the 5′-^{32}P SLII RNase V1 cleavage assays, we chemically synthesized short RNA markers which had the same sequence as SLII and had a 3′-OH. SLII markers were 10 (5′-GACAGUCGAU-3′) and 15 (5′-GACAGUCGAUGCAGG-3′) nucleotides in length (Figure 2, left). The oligomers were synthesized, purified and labeled in the same manner as SLII and SLIIc (see above). The other method used T4 polynucleotide kinase, in the absence of ATP, to remove the 3′-phosphate from the RNase T1 and alkaline hydrolysis products (19).

To quantify the footprinting data, we first normalized the total counts in each FinO–RNA complex lane to the total counts of the 'No Protein' lane to account for lane loading discrepancies. Then for each band of interest, representing a position in the RNA, the fraction (f) of the total counts for that band was calculated ($f_{p,\ i}$) where p is a FinO–RNA complex (either FinO, $FinO_{33–186}$ W36A or $FinO_{45–186}$), and i is the nucleotide position of the RNA. We also determined the fraction of the total counts for the 'No Protein' sample ($f_{np,i}$) at this position. Finally, we divide $f_{np,i}$ by $f_{p,i}$ to get the protection factor which is defined as the magnitude by which the RNA was protected from RNase cleavage by each FinO. For each RNase cleavage experiment, two independent reactions were performed and loaded onto the same gel. The values in Figures 2B and 3B are an average of these two independent reactions. We decided on a protection value of two or greater to represent a significant footprint. This is shown in the figures as a horizontal rule across the graph.

Preparation of samples for SAXS experiments

For the small-angle X-ray scattering (SAXS) experiments, the $FinO_{45–186}$ construct was the same as for the RNase footprinting studies. We used a full-length SLII construct with a different loop sequence denoted SLII LV1 (the sequence is shown in Figure 1C). The RNA was chemically synthesized and gel purified using the same procedures as for SLII and SLIIc (above). Precipitated RNA samples were resuspended in 1× TE pH 7.5, 10 mM NaCl at the appropriate concentration and quantified using extinction coefficients determined by an online calculator (Ambion).

SAXS data collection and analysis

SAXS data were collected at beamline 12.3.1 of the Advance Light Source, Lawrence Berkeley National Laboratory on a MAR165 detector (20,21), at a 1.6 m sample to detector distance and a wavelength of 1.12 Å. The hutch temperature was maintained at 17°C during

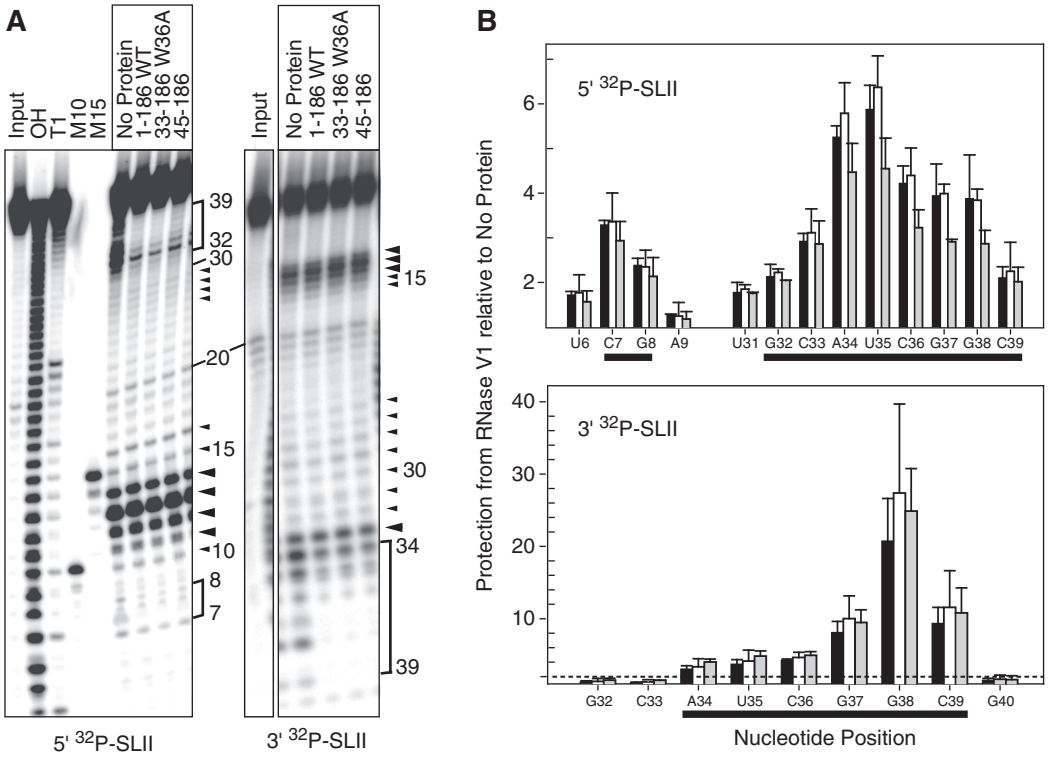

Figure 2. RNase V1 cleavage of 5′- and 3′-end-labeled SLII in the absence and presence of various FinO constructs. (**A**) 15% urea-denaturing polyacrylamide gels showing the products of RNase V1 (0.001 U/μl final concentration) cleavage reactions. M10 and M15 are synthesized SLII RNA markers of 10 and 15 nucleotides in length (see 'Materials and Methods' section). The lanes OH and T1 represent the alkaline hydrolysis and RNase T1 cleavage of denatured SLII, respectively. SLII nucleotide positions are indicated at the right of the gels. Large and small arrowheads indicate major or minor cleavages by RNase V1 in the presence of FinO. Vertical brackets represent significant footprints on SLII RNA resulting from FinO protection of SLII from RNase V1 attack. (**B**) Bar graphs showing the quantification of the footprint areas of the gels in (A). The left axis shows the degree of FinO protection from RNase V1 relative to the 'No protein' reaction. In black is $FinO_{1–186}$ WT, white is $FinO_{33–186}$ W36A, and in gray is $FinO_{45–186}$. Data above the horizontal dashed rule in each graph represent significant protection (≥2-fold) by FinO. The black bars below the *x*-axis highlight the footprint. The shift in the footprint when 5′- and 3′-end-labeling are compared is likely due to the effect of adding pCp to the 3′-end of the RNA when 3′-end-labeling. In Figure 6, we demonstrate that this subtly alters protein binding.

data collection. Solvent-only exposures of 7 and 70 s for background subtraction were taken from the dialysis supernatant of each construct before and after each sample data collection. A sequence of consecutive exposures lasting 7, 7, 70 and 7 s were recorded for each sample and the appropriate background exposure subtracted and circularly averaged using the program OGRE2 provided at the beamline. No sign of radiation-induced aggregation was observed in the consecutive exposures. The program AUTORG (22) was used to check the linearity of log(I(*s*)) versus s^2 at low angle ($s < 0.05\,\text{Å}^{-1}$) and confirm the absence of aggregation.

Protein–RNA docking

A model of SLII including the 5′- and 3′-tails was initially constructed based on the NMR structure of the initiator tRNA anti-codon loop from yeast, a 21-nt RNA stem–loop (RCSB accession code 1SZY) (23). The nucleotides were mutated to correspond to the sequence of SLII using COOT (24) and the stem–loop geometry-regularized in CNS (25). A model for $FinO_{45–186}$ was derived by removing residues 33–44 from the crystal structure (RCSB accession code 1DVO). The docking of SLII to $FinO_{45–186}$ was performed using the chemical restraint-driven program HADDOCK2.0 (26,27). On the protein, active ambiguous air restraints (AIRs) were defined as residues found to form chemical cross-links with the RNA as determined in Ghetu *et al.* (14) (Lys46, Lys81, Arg121, Lys125, Arg165 and Lys176). Passive AIRs on SLII were those nucleotides determined by ribonuclease footprinting to be protected in the complex, namely nucleotides 7, 8 and 36–45 (numbering as SLII in Figure 7A). No passive AIRS were defined for FinO, and no active AIRs were defined for SLII. Default settings were used for most HADDOCK parameters. No AIRs were randomly removed during separate docking trials. The stem of SLII was further geometry-restrained to be an A-form helix with Watson–Crick base pairing. The 5′- and 3′-tails of SLII were defined as both semi- and fully flexible regions. Semi-flexible protein residues were automatically chosen by HADDOCK if they were within 5.0 Å of the RNA. A control experiment was carried out, in which 2500 docking trials used randomly defined AIRs with random removal of 50% of AIRs per trial. Filtering of all docked models against the SAXS data used the program CRYSOL (28) to calculate theoretical scattering curves and obtain values of R_G and D_{max} for the models. The theoretical scattering curves were fit to the

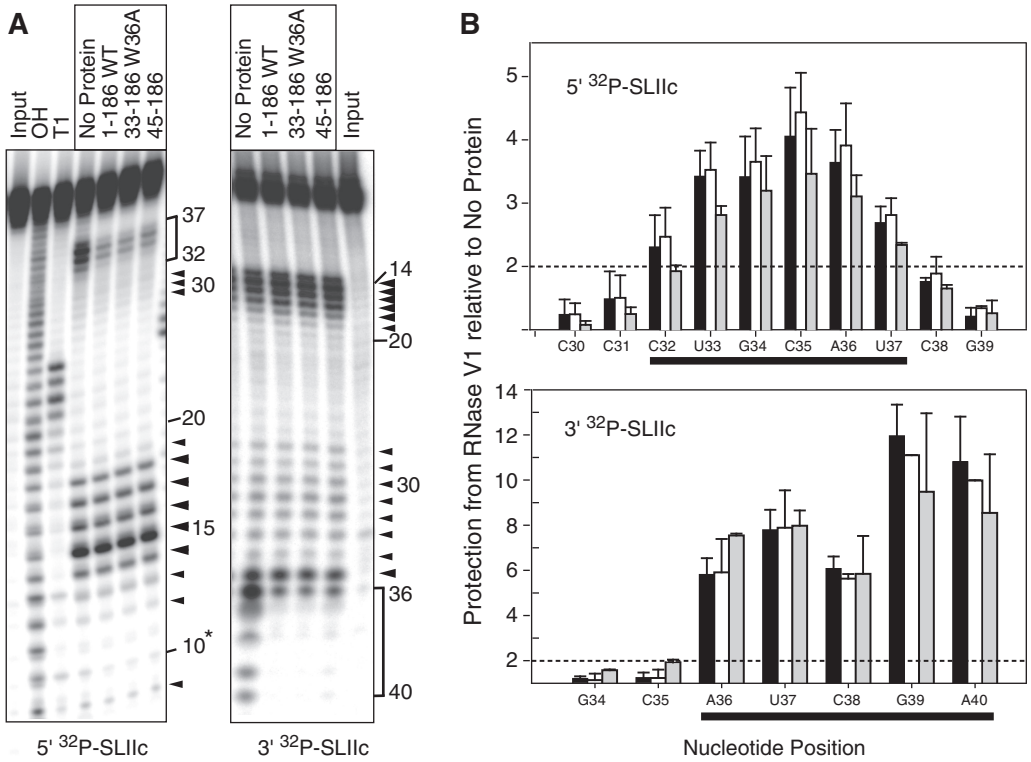

Figure 3. RNase V1 cleavage of 5′- and 3′-end-labeled SLIIc in the absence and presence of various FinO constructs. (**A**) 15% urea-denaturing polyacrylamide gels showing the products of RNase V1 (0.01 U) cleavage reactions. The lanes OH and T1 represent the alkaline hydrolysis and RNase T1 cleavage of denatured SLIIc, respectively. SLIIc nucleotide positions are indicated at the right of the gels. Large and small arrowheads indicate major or minor cleavages by RNase V1 in the presence of FinO. Vertical brackets represent significant footprints on SLIIc RNA resulting from FinO protection of SLIIc from RNase V1 attack. The asterisk at position C10 marks very weak protection of the lower stem at the 5′-end of SLIIc. (**B**) Bar graphs showing the quantification of the footprint areas of the gels in (A). The left axis shows the degree of FinO protection from RNase V1 relative to the 'No protein' reaction. In black is $FinO_{1–186}$ WT, white is $FinO_{33–186}$ W36A, and in gray is $FinO_{45–186}$. Data above the horizontal dashed rule in each graph represent significant protection (≥2-fold) by FinO. The black bars below the *x*-axis highlight the footprint.

experimental SAXS data using CRYSOL in the range $0 < s < 0.3\,Å^{-1}$ to provide a goodness-of-fit value, χ^2. The top 250 models, ordered on fit to the data, were subjected to pair-wise cluster analysis based on structural similarity. The RMSD cutoff of 13 Å was chosen as small as possible while still providing enough models in a cluster to be meaningful. The five clusters obtained had their members aligned using the maximum-likelihood superpositioning program THESEUS (29).

Calculation of electrostatic potentials

Electrostatic potentials were calculated using the Adaptive Poisson–Boltzmann Solver (30) and the PARSE force field. PDB2PQR was used to prepare the RCSB file 1DVO for this calculation (31).

RESULTS

FinO binds to the lower duplex region of SLII and SLIIc

In order to facilitate FinP–*traJ* mRNA pairing, FinO must first bind to its target RNAs. Previous studies have shown that FinO binds specifically and with high affinity to the SLII and SLIIc domains of FinP and *traJ* mRNAs, respectively (Figure 1A and B) (11,13). We used enzymatic footprinting experiments to determine which areas of these stem–loop target RNAs are contacted by FinO. We compared interactions made by full length FinO, with those of two mutants in which RNA strand exchange and duplexing have been compromised (Figure 1D). $FinO_{33–186\ W36A}$ lacks part of the N-terminal region required for RNA duplexing/strand exchange, and also bears a substitution at the critical Trp36 residue. This variant binds RNA with a significantly enhanced affinity, but its strand exchange and duplexing activities are reduced compared to wild-type FinO. $FinO_{45–186}$ corresponds to the core RNA binding domain and binds SLII with a 20-fold higher affinity than wild-type FinO, but has no detectable strand exchange or RNA duplexing activity.

RNase V1 (32) was used to map interactions between the various FinO proteins and double-stranded or stacked single-stranded regions of RNA targets. SLII and SLIIc RNAs were radiolabeled at the 5′- or 3′-end and subjected to limited RNase V1 digestion alone or in complex with FinO at a 1:1 molar ratio. Native gel electrophoresis was used to ensure complex formation under these conditions (Figure 1E). The results of the RNase V1 cleavage experiments with 5′ and 3′-end-labeled SLII are shown in Figure 2A. In the absence of FinO, strong cleavage was observed on both strands of the duplex stem, consistent

with previous ribonuclease mapping carried out on intact FinP (33). FinO binding protected residues G32-C39 on 5′-^{32}P-SLII (left gel) and residues A34-C39 on 3′-^{32}P-SLII (right gel) corresponding to the lower 3′-portion of the SLII double-stranded stem region. A minor footprint was observed on the 5′-^{32}P-SLII gel at positions C7 and G8, which maps to the lower 5′-portion of the SLII stem. Essentially identical protection patterns were observed for all three FinO constructs. Quantification of the footprint regions is shown in Figure 2B. For this study, we chose protection values greater than or equal to 2-fold relative to the 'No Protein' sample as significant (see 'Materials and Methods' section).

An area of intense RNase V1 cleavage was observed on the 5′-side of the SLII stem proximal to the loop (residues G11–G14, with minor cleavages at U10 and G15–G16) in the presence of all FinO constructs. Minor cleavages also were observed on the 3′-side of the SLII stem proximal to the loop (C26 to G32). Taken together, the results suggest that FinO contacts the end of the SLII duplex proximal to the single-stranded tails but does not contact the region of the stem proximal to the loop.

The RNase V1 cleavage results for SLIIc were similar for SLII (Figure 3). FinO protected the lower portion of the 3′-side of the stem of SLIIc from RNase V1 cleavage at positions C32-U37 on 5′-^{32}P-SLIIc and A36-A40 on 3′-^{32}P-SLIIc. Like SLII, there appeared to be a very weak protection of the lower stem at the 5′-end of SLIIc at position C10 (marked by an asterisk in Figure 3A, left gel). Both 5′- and 3′-end-labeled SLIIc gels have strong RNase V1 cleavages at the upper portion of the stem on the 5′ side. These cleavages at positions C14 to G18, with weaker cleavages nearby, were observed in the presence of all FinO constructs. The upper 3′ portion of the SLIIc stem had weaker cleavages from C28 to G34. The results indicate that SLIIc binds to FinO and its derivatives in a similar fashion as SLII, with the interaction occurring at the lower part of the SLIIc stem region, leaving the upper half of the stem exposed to cleavage by RNase V1.

FinO does not bind to the loop region of its target RNAs

It was previously shown that deletion of the seven nucleotide loop from SLII does not affect the affinity of FinO binding, suggesting the loop plays little if any role in specific, high affinity interactions with FinO (15). We used RNase I (34) footprinting to directly probe for interactions between FinO and single-stranded areas of SLII or SLIIc. Figure 4 shows the results for the limited RNase I digestion of SLII and SLIIc both free, and in a 1:1 complex with the three FinO constructs. For both RNAs, intense cleavage was observed, as expected, at the single-stranded loop regions, and FinO binding consistently resulted in a significant enhancement in this cleavage.

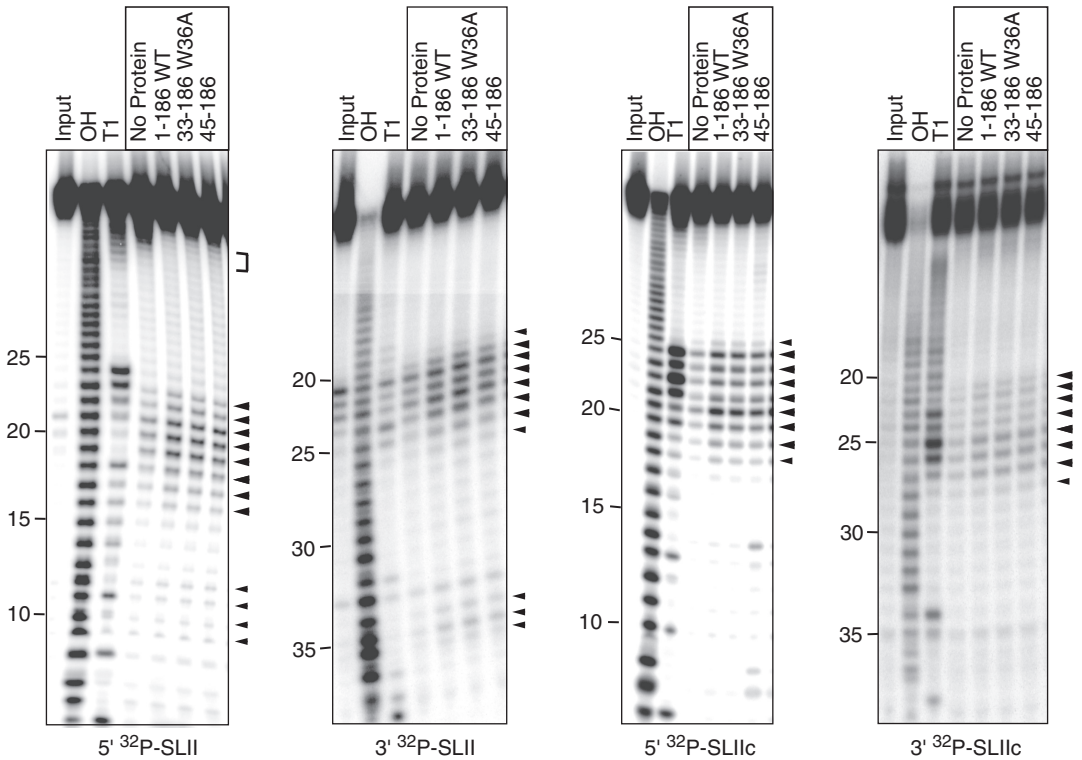

Figure 4. Limited RNase I digestion of 5′- and 3′-end-labeled SLII and SLIIc in the absence and presence of various FinO constructs. Products of the RNase I (0.01 U/μl final concentration) cleavage reactions were resolved on 15% urea-denaturing polyacrylamide gels. The radiolabeled RNA construct is noted below each of the gels. The lanes OH and T1 represent the alkaline hydrolysis and RNase T1 cleavage of denatured SLII or SLIIc, respectively. The RNA nucleotide positions are indicated at the left of the gels. Large and small arrowheads indicate major or minor cleavages by RNase I in the presence of FinO while the vertical bracket indicates protection from RNase I.

FinO protects the 3′-tails of SLII and SLIIc from RNase I degradation and enhances cleavage of the 5′-tail of SLIIc

It has been shown by electrophoretic mobility shift assays that a 3′ single-stranded tail of at least six nucleotides on SLII (and FinP) is required to bind FinO (11). Removing the tail in its entirety led to a 5.5-fold decrease in affinity for FinO-GST. To a much lesser extent, removing the four nucleotide 5′-tail of SLII (spacer between SLI and SLII in FinP) led to a modest 1.3-fold decrease in affinity, and removal of both tails decreased affinity for FinO by nearly 14-fold. We used RNase I footprinting to test for interactions between FinO and the 5′- and 3′-tails. The 5′-^{32}P-labeled SLII cleavage gel in Figure 4 suggests that protection of the 3′-tail does occur.

To more clearly assess this protection, we carried out RNase I footprinting experiments at a much higher RNase I concentration, to enhance cleavage of the 3′-tail and reduce the amount of full-length RNA which would otherwise obscure the footprint. The clearest results were obtained for 5′-labeled SLII RNA (Figure 5A). Under these conditions, the 3′-tail was completely removed in the absence of FinO. Dramatic protection was observed with increasing FinO concentrations, suggesting a strong interaction between FinO and the 3′-tail. Less dramatic but significant protection was observed for the 3′-tail of SLIIc (Figure 5B). Similar results were also observed for $FinO_{33–186}$ W36A and $FinO_{45–186}$ (data not shown).

In contrast, the 5′-tails of SLII and SLIIc did not appear to be protected by FinO. This was most clearly demonstrated for the SLIIc construct (Figure 5C). Here, modest cleavage of the 5′-tail was observed in the absence of FinO, however, binding of any of the FinO variants resulted in a more significant cleavage of the 5′-tail. This suggests that FinO binding frees the 5′-tail of SLIIc for attack by RNase I. We were unable to detect RNase I cleavage at the shorter, four nucleotide 5′-tail of SLII (Figure 5D). A summary of the RNase I and RNase VI cleavage data for SLII and SLIIc is shown in Figure 7A.

FinO selectively binds to the 3′-hydroxyl group of the 3′-tail of SLII

To further test the nature of recognition of the SLII 3′-tail by FinO, we created a version of SLII in which 3′,5′-cytidine diphosphate (pCp) was appended at the

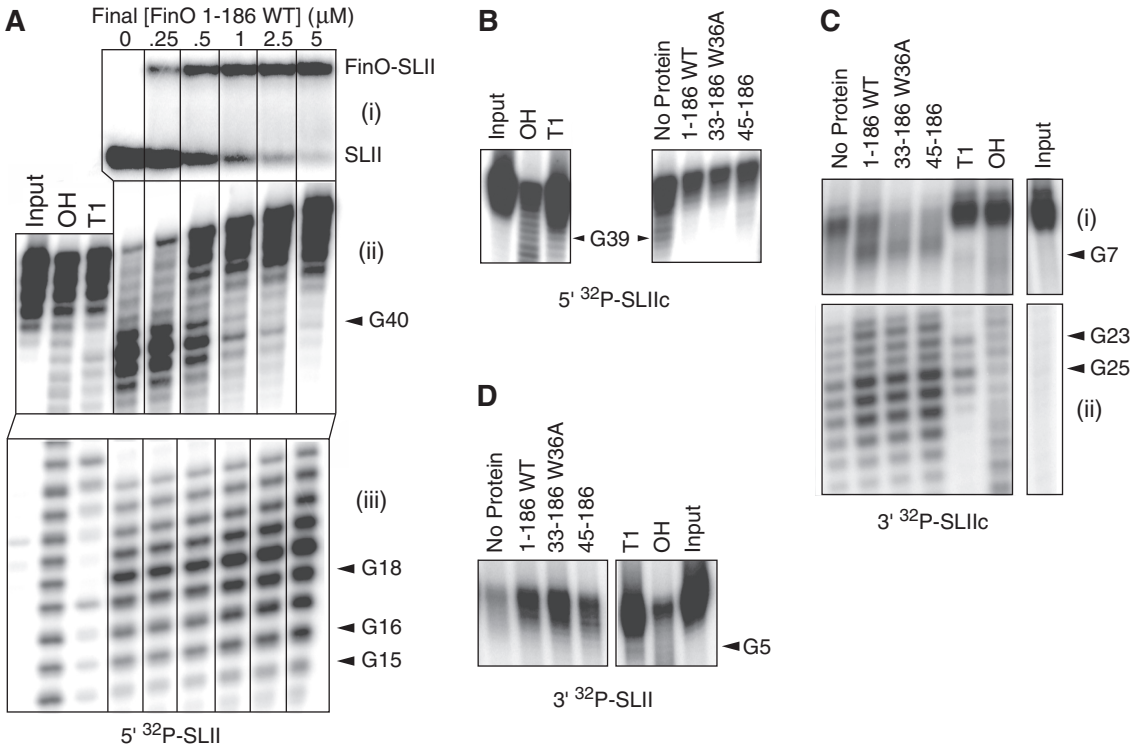

Figure 5. RNase I overdigestion of 5′- and 3′-end-labeled SLII and SLIIc in absence and presence of various FinO constructs. In all experiments, the RNAs were digested with RNase I at a final concentration of 0.1 U/μl. (**Ai**) A 8% native EMSA showing binding reactions of 5′-^{32}P-SLII with increasing amounts of wild-type FinO before the addition of RNase I. The final concentration of FinO WT in micromolar in each reaction is indicated on top of the gel. (Aii) Slice from a 15% urea-denaturing gel showing the products of the RNase I digest of 5′-^{32}P-SLII at the 3′-end in the presence of increasing amounts of FinO. The lanes correspond to the binding reactions in (Ai). The lanes OH and T1 represent the alkaline hydrolysis and RNase T1 cleavage of denatured 5′-^{32}P-SLII, respectively. SLII nucleotide positions are indicated at the right of the gel. (**B**) Slice from a 15% urea-denaturing gel showing the products of the RNase I digest of 5′-^{32}P-SLIIc at the 3′-end in the absence and presence of various FinO constructs. Nucleotide position G39 is indicated next to the gel. (**C**) Slice from a 15% urea-denaturing gel showing the products of the RNase I digest of 3′-^{32}P-SLIIc at the 5′-end in the absence and presence of various FinO constructs. SLIIc nucleotide positions are indicated next to the gel. (**D**) Slice from a 15% urea-denaturing gel showing the products of the RNase I digest of 3′-^{32}P-SLII at the 5′-end in the absence and presence of various FinO constructs. Nucleotide position G5 is indicated at the right of the gel. For experiments in (B–D), a 1:1 molar ratio FinO-RNA complex was formed prior to exposure to RNase I.

3′-end using T4 RNA ligase I. Intriguingly, none of the FinO constructs bound this RNA in electrophoretic mobility shift assays; however, binding could be restored by treatment of this RNA with T4 kinase/phosphatase to remove the terminal 3′-phosphate (Figure 6). To further probe the specificity for the RNA 3′-hydroxyl group, we next treated the RNA with $NaIO_4$, which selectively oxidizes the 3′ ribose sugar to a 2′,3′ dialdehyde (35). This treatment abrogated FinO binding, further demonstrating the selective recognition of the 3′-hydroxyl group by FinO.

An energy-minimized, biochemical knowledge-driven model of the $FinO_{45–186}$–SLII complex

High resolution structural information for FinO–RNA complexes has been difficult to obtain using either X-ray crystallographic or NMR approaches (D.C.A., R.A.E. and J.N.M.G., unpublished data). In the absence of such information, we turned to small-angle X-ray scattering (SAXS) to provide structural information to help to define FinO–RNA interactions, as it is suitable to define flexible and dynamic complexes (36). We decided to focus on complexes between $FinO_{45-186}$ and the minimal SLII RNA target for three reasons. First, the footprinting results described above indicate that $FinO_{45–186}$ contacts the same regions within stem-loop RNA targets as full-length FinO. Second, $FinO_{45–186}$ is more soluble and less prone to aggregation than the larger FinO constructs, and therefore is more appropriate for SAXS measurements. Third, the fact that $FinO_{45–186}$ binds SLII with ~20-fold higher affinity than full-length FinO helps ensure that the experimental sample is fully bound under the SAXS solution conditions and does not contain a significant fraction of unbound components. SAXS data were collected at the SIBYLS beamline at the Advanced Light Source on $FinO_{45–186}$ with the minimal SLII RNA target. Analysis was consistent with complex formation.

In order to present a rigorous structural model of the $FinO_{45–186}$–SLII interaction, we docked existing X-ray crystal structures of the individual components in a restrained energy-minimization procedure. The restraints were derived from biochemical information presented here and in previous work (14). A number of spatially different models resulted, all consistent with the input restraints. These models were then further filtered based on their agreement to the solution scattering profile of the $FinO_{45–186}$–SLII complex. A single orientation of the RNA stem–loop docked on FinO agreed with both the biochemical and SAXS data. The restrained energy minimization was carried out using the program HADDOCK (26,27).

Docking in HADDOCK is a multi-step procedure consisting of rigid-body docking by energy minimization, torsion-angle refinement of residues or nucleotides involved in the docking interface, and a final Cartesian dynamics refinement in water. The energy minimization is constrained by chemical distance restraints called AIRs. AIRs are defined by the user from knowledge derived from biochemical or biophysical experiments about the docking components and their interactions. We have used a combination of site-directed protein–RNA cross-linking (14) and RNA footprinting (this work) to define AIRs between the protein and the RNA. The RNA footprinting results define regions of the RNA that are protected from ribonuclease digestion by FinO and are therefore likely involved in, or adjacent to, the protein–RNA interface. The protein–RNA cross-linking data defines which regions of the protein are in close enough proximity to the RNA to form a chemical cross-link. The crosslinker used, azidophenacyl bromide, reacts non-specifically with RNA within a 10 Å radius. In HADDOCK, two types of AIRs are formally defined, active and passive. Active restraints are between residues shown experimentally to be involved in the interaction and have a solvent-exposed surface area of >50%. Passive restraints are between similarly solvent-exposed residues that are direct neighbors of active residues. Distance restraints during the energy-minimization are applied between pairs of residues being either active–active or active–passive, but not passive–passive combinations.

Six protein residues showed appreciable cross-linking to the RNA and were assigned as active AIRs on the protein. Notably, Arg121 and Lys125, both part of a positively charged patch on one side of the base of FinO, exhibited significantly stronger crosslinks than Lys46, Lys81, Arg165 or Lys176. Nucleotides of SLII protected from

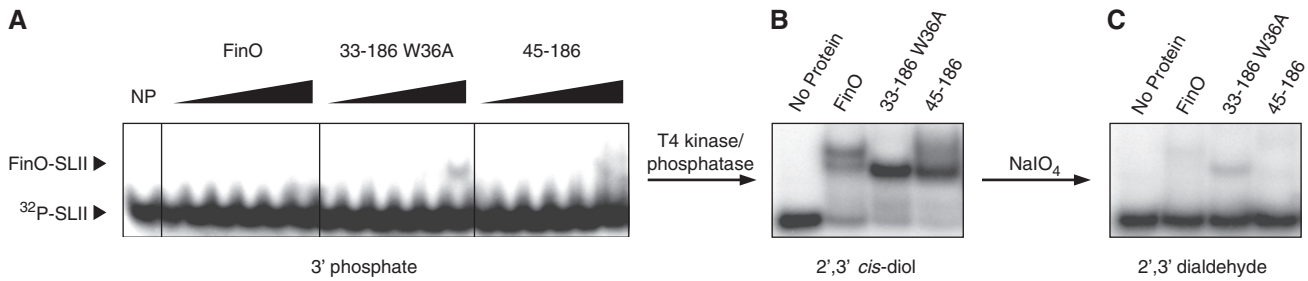

Figure 6. FinO binding to SLII requires a terminal 3′-OH on the 3′-tail of SLII. Native gels (8%) of binding reactions between FinO constructs and SLII RNA derivatives. (**A**) FinO does not bind SLII RNA containing a 3′,5′-cytidine diphosphate 3′-terminus. T4 RNA ligase I was used to ligate 3′,5′-cytidine [5′-^{32}P] disphosphate (pCp) to the 3′-tail resulting in a 3′-phosphate. NP, no protein. Triangles represent increasing concentrations of FinO or the indicated mutants: 0.25, 0.5, 1, 2.5, 5 and 10 μM. The positions of free ^{32}P-SLII and the FinO-^{32}P-SLII are noted by arrows. (**B**) Treatment of SLII RNA containing a 3′,5′-cytidine diphosphate 3′-terminus to give a 2′,3′ *cis*-diol (3′-hydroxyl) restores FinO binding. (**C**) Oxidation of SLII with sodium periodate to give a 2′,3′ dialdehyde reduces binding affinity. The protein concentrations were 1 μM in each of the binding reactions in B and C.

RNaseV1 or RNase I cleavage upon FinO binding (7,8,36–45, Figure 7A), were assigned as passive AIRs.

HADDOCK was used to generate 2500 models sampling a subset of the complex's conformation space defined by the biochemical information encoded in the form of ambiguous interaction restraints (see 'Materials and Methods' section). RNA duplexes were primarily restricted to the positively charged face of the protein and oriented with the 5′-and 3′-tails contacting the base of FinO with the loop exposed into the solvent, orientations

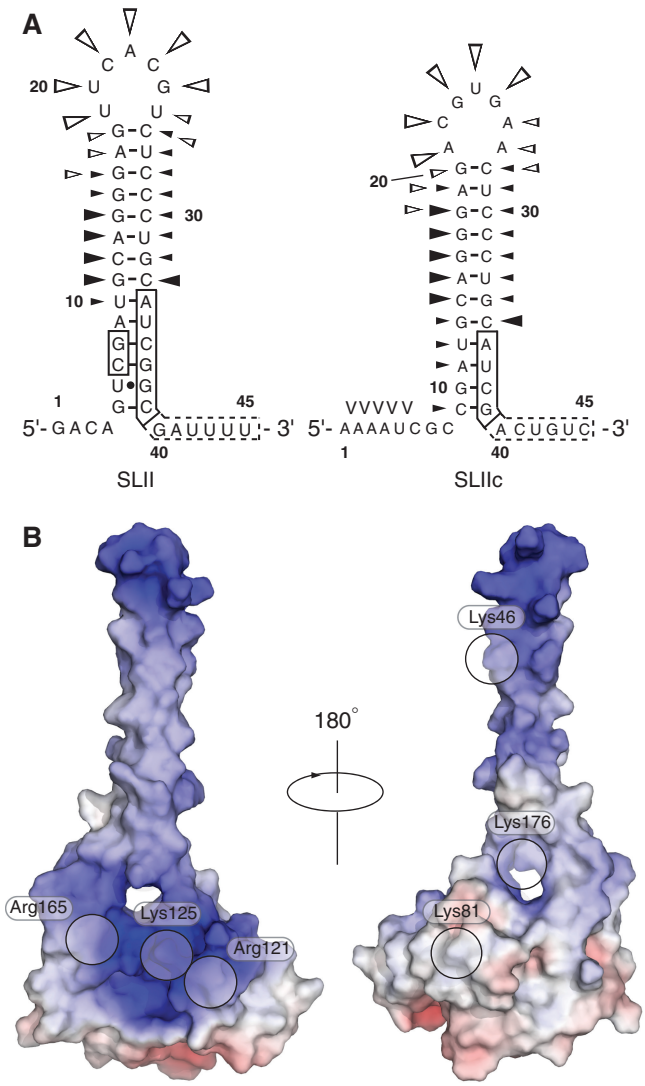

Figure 7. Summary of RNase V1 and I cleavage reactions of SLII and SLIIc. (**A**) Secondary structures of SLII and SLIIc showing the results from the RNase cleavage reactions. Large and small black arrowheads denote strong and weak RNase V1 cleavages, respectively in the presence of the FinO constructs. Large and small open arrowheads denote strong and weak RNase I cleavages, respectively in the presence of FinO. Boxes indicate footprints where FinO protected the RNAs from RNase V1 cleavage. Dashed boxes indicate areas of protection from RNase I cleavage by FinO. An area where a 'V' resides indicates enhanced cleavage by RNase I in the presence of the FinO constructs. (**B**) Electrostatic potentials at the solvent accessible surface of $FinO_{33–184}$, contoured at ±10 kT/e. Approximate surface locations of the six FinO side-chains known to cross-link to SLII are labeled and shown with semi-transparent circles.

largely constrained by the distance restraints. The models sample a broad selection of size and shape, with R_G ranging from 23.0 to 33.9 Å. The mean fit to the data for this model set had a χ^2 of 11.5 with a best fit of 3.4. A further improvement in fit could be obtained by allowing those residues determined to be flexible by normal mode analysis of $FinO_{45–186}$, namely residues 45–64 of the N-terminal α-helix, to be fully flexible during the docking. This flexible model set had a mean and best fit χ^2 of 9.7 and 2.3, respectively. The full model set is represented in Supplementary Figure 1 along with a subset of the best 50 models ordered on χ^2.

For comparison, HADDOCK was run using randomly selected AIRs between residues and nucleotides containing >20% relative accessibility to generate 2500 models. This random-AIR model set had a mean χ^2 of 17.5, significantly worse than that of the restrained model set, with the single best-fit to the experimental scattering of 2.1. Although this best-fit randomly restrained model slightly improves the fit to the SAXS data relative to the best-fit restrained model, inspection shows a poor fit to the biochemical data. The best 250 RNA–protein complex models, ordered on χ^2 were subjected to RMSD-based pair-wise cluster analysis. Five clusters (Figure 8) met the criteria of having a pair-wise RMSD cutoff less than 13 Å and containing at least six members. In every case, the RNA docked to the side of FinO containing the positively charged patch and residues Arg121, Lys125 and Arg165. Alignment of the stem–loop was also consistent amongst all clusters with the base of the RNA closer to the globular portion of FinO and the stem-loop generally coincident with the N-terminal helical extension. A representative model from one of these clusters was chosen to illustrate the satisfaction of a number of the programmed distance restraints and the general orientation of the RNA stem (Figure 9A) while still providing a reasonable fit to the SAXS data (Figure 9B). Nucleotides C7 and G8 are partially buried against the N-terminal α-helix of FinO and the 3′-tail extends along the positively charged face of FinO within contact distance of residues Arg121, Lys125 and Arg165. The fit of this particular model to the experimental data, χ^2 of 4.2, is comparable to the mean χ^2 of 4.6 for all 39 models in the five clusters.

DISCUSSION

FinO binds to SLII and SLIIc at the lower half of the duplex and the 3′-tail

Our footprinting results indicate that FinO binds its target RNAs through recognition of single strand–duplex RNA junctions. This interaction is asymmetric; that is, the 3′ single strand and 3′ side of the duplex is contacted more strongly by the protein than the 5′ single-stranded tail or the 5′ side of the duplex. While these interactions were clearly evident in ribonuclease footprinting experiments, we were unable to detect any interactions using the chemical probes diethylpyrocarbonate (DEPC), dimethylsulphate (DMS), or hydroxyl radical (data not shown). This suggests that FinO does not interact tightly with the bases or sugars of the RNA, and largely relies on

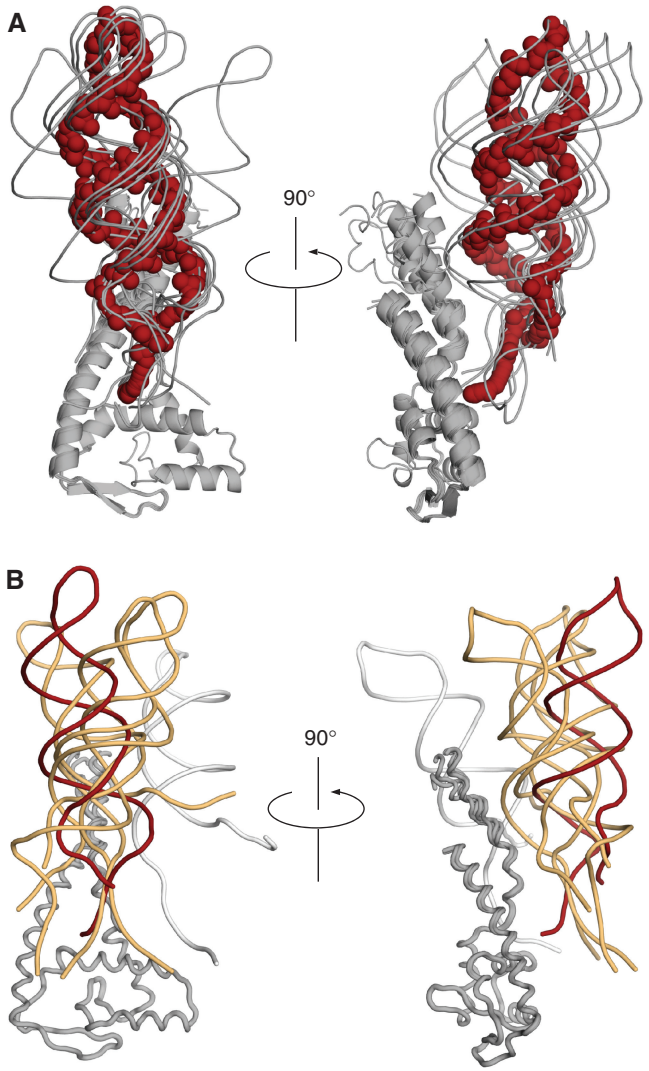

Figure 8. Combining HADDOCK and SAXS to model $FinO_{45–186}$:SLII. Pair-wise RMSD cluster analysis was performed on the top 250 models ordered on χ^2. Five clusters were obtained using an RMSD cutoff of 13 Å. (**A**) Model complexes from the best cluster (mean χ^2 for nine members, 4.1) are shown in gray. The average structure for this cluster as calculated using THESEUS is represented with red spheres. (**B**) The average structures for all five clusters are shown superimposed. The average structure for the best cluster shown in (A) is shown as a red ribbon, and that of a significant structural outlier in white.

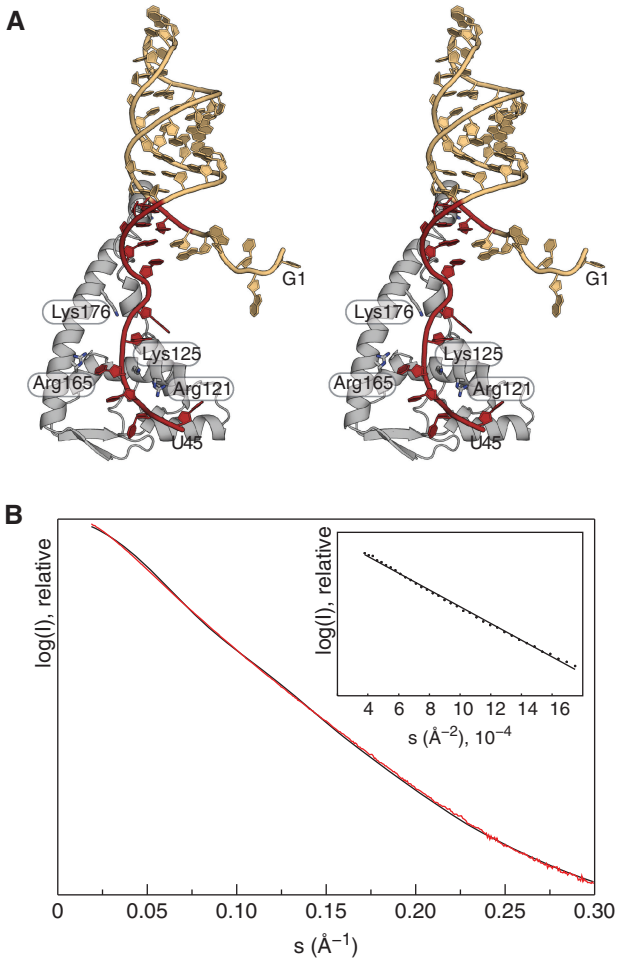

Figure 9. Representative $FinO_{45–186}$:SLII model. (**A**) Shown in stereo, a cartoon representation of one of the individual FinO–SLII complexes from the cluster analysis. Nucleotides 7, 8 and 34–45, which are protected from RNase I and VI cleavage upon complex formation, are shown in red. Side-chains of cross-linking residues Arg121, Lys125, Arg165 and Lys176 are all within contact distance of the single-stranded 3′-tail. (**B**) The theoretically calculated small-angle X-ray scattering curve (black) of the model shown in (A) fits the experimental data curve (red) with a χ^2 of 4.2. Inset, the Guinier plot of experimental data points 2–36 ($s.R_G$ 0.61–1.29), the linear nature of which indicates a lack of aggregation in the sample.

electrostatic interactions between the large number of positively charged residues on the surface of FinO and the RNA phosphate groups. This is consistent with the finding that, while FinO requires its targets to contain a duplex-single strand junction, the precise sequence of the RNA target appears to be less critical (11).

While our footprinting and cross-linking data identified areas of SLII and SLIIc which are contacted by FinO, and highlighted which areas of FinO contact SLII, these data alone do not directly reveal the orientation of the stem–loop on FinO. In the absence of high resolution structural information, we chose SAXS to guide our structural modeling of the FinO–RNA complex. SAXS is a low resolution, solution technique able to provide information on flexible complexes (36,37) and can be particularly powerful when applied to restrain the docking of known structures (21). We used biochemical constraints from the RNase footprinting data presented here and site-specific FinO–RNA cross-linking studies (14) to guide the generation of a large set of docked test models composed of $FinO_{45–186}$ and the tailed SLII duplex. Molecular dynamics was employed during the docking procedure to provide conformational flexibility for the single stranded tails of the RNA. The resulting models were then ranked based on their fit to experimental SAXS data for this complex. This procedure distinguished a cluster of conformationally similar models that fit the SAXS data much better than the other models. In the best fit model obtained from this procedure, FinO lies against the 3′ single strand and 3′ side of the duplex in a manner that at once accounts for the RNase protection

patterns as well as site specific FinO–RNA cross-linking data. The upper portions of the stem–loop are solvent exposed and the stem–loop is oriented anti-parallel to the N-terminal α-helix of FinO. While stem-loop orientations in other directions may fit the footprint and cross-link data to varying degrees, only complexes having the general stem–loop orientation shown in the clusters (Figure 8B) fit both these data and the SAXS data. Hence, SAXS allows us to break the ambiguity of RNA orientation on FinO.

Intriguingly, we also demonstrate that either phosphorylation or oxidation of the 3′-nucleotide of SLII abrogates FinO binding, suggesting that FinO selectively recognizes the 3′-nucleotide of the target RNA in a manner that requires a free 3′-hydroxyl group. This suggests that primary FinO RNA targets will be found near the 3′-terminus of transcripts, as is the case for FinP SLII; however, stem–loops buried within larger RNAs, such as SLIIc within *traJ* mRNA, may be recognized less efficiently. The La protein also binds RNA transcripts in a manner that relies on the presence of a 3′-hydroxyl group (38). Selective binding of 3′-hydroxyl versus 3′-phosphate transcripts by La is mediated in part by a conserved aspartic acid that may select against the negatively charged 3′-phosphate. La binding at the 3′-end of pol III transcripts protects these RNAs from exonucleolytic degradation. While FinO also protects FinP against degradation *in vivo*, the degradation is catalyzed by the endonuclease RNase E, and exonucleases such as PNPase and RNase II are likely not involved (8).

Implications for the molecular mechanism of FinO RNA chaperone function

$FinO_{45–186}$ is responsible for stable, high affinity recognition of its specific RNA substrates; however, this region is completely unable to facilitate FinP–*traJ* interactions. Instead, the highly flexible N-terminal regions are absolutely essential for this function. These regions do contact the RNA, as indicated by site-specific protein–RNA cross-linking (14). The N-terminal regions likely do not contact regions of the RNA target outside that bound by $FinO_{45–186}$, since the footprints obtained with full-length FinO and $FinO_{45–186}$ are identical. We suggest that the N-terminal region, which adopts an extended conformation in the crystal structure of the free protein, collapses around the RNA to contact the base of the stem and/or the 3′ single-stranded region. This rearrangement is supported by in-gel fluorescence resonance energy transfer (FRET) experiments that suggest that residues 37 and 42 within this region (KWK_{37} $KVKKQK_{42}$) come into relatively close contact with the single-stranded tails of an SLII-like RNA, but not with regions of the duplex close to the hairpin loop (14). This rearrangement could bring Trp36, which appears to be the single residue most critical for RNA annealing and chaperone activity (15), into contact with the duplex-single-stranded junction, potentially to stack with exposed bases in this region. Stacking between hydrophobic amino acid side chains and nucleotide bases are a common feature of protein–RNA recognition processes, especially for proteins which recognize substrates containing duplex-single-stranded junctions (39,40).

Disordered or highly dynamic protein domains are thought to be a common hallmark of many RNA chaperones, such as hnRNP A1 (41) and HIV nucleocapsid protein (42). An ‘entropy transfer model’ for chaperone function has been proposed in which structural disorder in the unbound chaperone is transferred to the RNA substrate upon binding, increasing the flexibility of the RNA and aiding in RNA refolding processes (43). Intriguingly, there appears to be an inverse correlation between the chaperone activity of FinO mutants and their RNA binding affinities. $FinO_{45–186}$, which has no detectable chaperone activity, binds RNA 20-fold more tightly than full-length FinO, while $FinO_{26–186}$, which has a more modest 10-fold decrease in the rate of RNA strand annealing, also shows a lesser, 4-fold increase in RNA binding affinity compared to full-length (15). We suggest that RNA binding may provide free energy required for RNA remodeling, consistent with the entropy transfer model. In this way, $FinO_{45–186}$ may anchor the initial binding process and facilitate the subsequent action of the N-terminal chaperone domain.

FinO defines a new family of bacterial RNA chaperones

The best studied RNA chaperone in bacterial systems is Hfq, an Sm domain protein that adopts a hexameric ring structure and binds AU-rich RNA targets on one side of the ring (44). Mechanistically, Hfq likely functions differently than FinO. Whereas Hfq, like FinO, exhibits RNA annealing activity, it does not exhibit strong RNA strand exchange activity (45).

Searches of protein sequence databases reveals that the *E. coli* protein ProQ, a post-transcriptional regulator of osmotic stress (46,47), contains a domain with 25% sequence identity to $FinO_{45–186}$ (48,49). Intriguingly, ProQ contains a second domain with similarity to Sm domain proteins. Thus, ProQ may act as novel, two-domain chaperone in *E. coli*. While sequence-based searches do not reveal other proteins with similarity to FinO, protein structure similarity searches reveal that the *Neisseria meningitidis* protein NMB1681 (PDB code 2HXJ) bears striking similarity to $FinO_{45-186}$, with additional flexible N- and C-terminal regions. It is therefore possible that FinO is not a unique RNA chaperone, but may be a member of a larger family of chaperones that function in many bacterial species to regulate diverse small RNA-mediated processes.

SUPPLEMENTARY DATA

Supplementary Data are available NAR Online.

ACKNOWLEDGEMENTS

We thank Andrew MacMillan for helpful discussions.

FUNDING

Canadian Institutes of Health Research (CIHR); the Howard Hughes Medical Institute (HHMI) International Scholar Program (to J.N.M.G.); SAXS beamline SIBLYS and efforts on complexes controlling microbial colonies funded by the MAGGIE (Molecular Assemblies, Genes and Genomes Integrated Efficiently) project, Department of Energy grant (DE-FG0207ER64326 to J.A.T.) in part. Funding for open access charge: Canadian Institutes of Health Research (CIHR).

Conflict of interest statement. None declared.

REFERENCES

1. Ippen-Ihler,K.A. and Minkley,E.G. Jr (1986) The conjugation system of F, the fertility factor of *Escherichia coli*. *Annu. Rev. Genet.*, **20**, 593–624.
2. Frost,L.S., Ippen-Ihler,K. and Skurray,R.A. (1994) Analysis of the sequence and gene products of the transfer region of the F sex factor. *Microbiol. Rev.*, **58**, 162–210.
3. Finnegan,D. and Willetts,N. (1972) The nature of the transfer inhibitor of several F-like plasmids. *Mol. Gen. Genet.*, **119**, 57–66.
4. Finnegan,D. and Willetts,N. (1973) The site of action of the F transfer inhibitor. *Mol. Gen. Genet.*, **127**, 307–316.
5. Gaffney,D., Skurray,R. and Willetts,N. (1983) Regulation of the F conjugation genes studied by hybridization and tra-lacZ fusion. *J. Mol. Biol.*, **168**, 103–122.
6. Willetts,N. (1977) The transcriptional control of fertility in F-like plasmids. *J. Mol. Biol.*, **112**, 141–148.
7. Will,W.R. and Frost,L.S. (2006) Characterization of the opposing roles of H-NS and TraJ in transcriptional regulation of the F-plasmid tra operon. *J. Bacteriol.*, **188**, 507–514.
8. Jerome,L.J., van Biesen,T. and Frost,L.S. (1999) Degradation of FinP antisense RNA from F-like plasmids: the RNA-binding protein, FinO, protects FinP from ribonuclease E. *J. Mol. Biol.*, **285**, 1457–1473.
9. Lee,S.H., Frost,L.S. and Paranchych,W. (1992) FinOP repression of the F plasmid involves extension of the half-life of FinP antisense RNA by FinO. *Mol. Gen. Genet.*, **235**, 131–139.
10. van Biesen,T. and Frost,L.S. (1994) The FinO protein of IncF plasmids binds FinP antisense RNA and its target, traJ mRNA, and promotes duplex formation. *Mol. Microbiol.*, **14**, 427–436.
11. Jerome,L.J. and Frost,L.S. (1999) In vitro analysis of the interaction between the FinO protein and FinP antisense RNA of F-like conjugative plasmids. *J. Biol. Chem.*, **274**, 10356–10362.
12. Ghetu,A.F., Gubbins,M.J., Frost,L.S. and Glover,J.N. (2000) Crystal structure of the bacterial conjugation repressor finO. *Nat. Struct. Biol.*, **7**, 565–569.
13. Ghetu,A.F., Gubbins,M.J., Oikawa,K., Kay,C.M., Frost,L.S. and Glover,J.N. (1999) The FinO repressor of bacterial conjugation contains two RNA binding regions. *Biochemistry*, **38**, 14036–14044.
14. Ghetu,A.F., Arthur,D.C., Kerppola,T.K. and Glover,J.N. (2002) Probing FinO-FinP RNA interactions by site-directed protein-RNA crosslinking and gelFRET. *RNA*, **8**, 816–823.
15. Arthur,D.C., Ghetu,A.F., Gubbins,M.J., Edwards,R.A., Frost,L.S. and Glover,J.N. (2003) FinO is an RNA chaperone that facilitates sense-antisense RNA interactions. *EMBO J.*, **22**, 6346–6355.
16. Sandercock,J.R. and Frost,L.S. (1998) Analysis of the major domains of the F fertility inhibition protein, FinO. *Mol. Gen. Genet.*, **259**, 622–629.
17. Ho,S.N., Hunt,H.D., Horton,R.M., Pullen,J.K. and Pease,L.R. (1989) Site-directed mutagenesis by overlap extension using the polymerase chain reaction. *Gene*, **77**, 51–59.
18. Scaringe,S.A. (2001) RNA oligonucleotide synthesis via 5′-silyl-2′-orthoester chemistry. *Methods*, **23**, 206–217.
19. Brown,T.S. and Bevilacqua,P.C. (2005) Method for assigning double-stranded RNA structures. *Biotechniques*, **38**, 368, 370, 372.
20. Hura,G.L., Menon,A.L., Hammel,M., Rambo,R.P., Poole,F.L. II, Tsutakawa,S.E., Jenney,F.E. Jr, Classen,S., Frankel,K.A., Hopkins,R.C. *et al.* (2009) Robust, high-throughput solution structural analyses by small angle X-ray scattering (SAXS). *Nat. Methods*, **6**, 606–612.
21. Putnam,C.D., Hammel,M., Hura,G.L. and Tainer,J.A. (2007) X-ray solution scattering (SAXS) combined with crystallography and computation: defining accurate macromolecular structures, conformations and assemblies in solution. *Q. Rev. Biophys.*, **40**, 191–285.
22. Petoukhov,M.V., Konarev,P.V., Kikhney,A.G. and Svergun,D.I. (2007) ATSAS 2.1 – towards automated and web-supported small-angle scattering data analysis. *J. Appl. Cryst.*, **40**, s223–s228.
23. Schweisguth,D.C. and Moore,P.B. (1997) On the conformation of the anticodon loops of initiator and elongator methionine tRNAs. *J. Mol. Biol.*, **267**, 505–519.
24. Emsley,P. and Cowtan,K. (2004) Coot: model-building tools for molecular graphics. *Acta Crystallogr. D Biol. Crystallogr.*, **60**, 2126–2132.
25. Brunger,A.T., Adams,P.D., Clore,G.M., DeLano,W.L., Gros,P., Grosse-Kunstleve,R.W., Jiang,J.S., Kuszewski,J., Nilges,M., Pannu,N.S. *et al.* (1998) Crystallography & NMR system: a new software suite for macromolecular structure determination. *Acta Crystallogr. D Biol. Crystallogr.*, **54**, 905–921.
26. de Vries,S.J., van Dijk,A.D., Krzeminski,M., van Dijk,M., Thureau,A., Hsu,V., Wassenaar,T. and Bonvin,A.M. (2007) HADDOCK versus HADDOCK: new features and performance of HADDOCK2.0 on the CAPRI targets. *Proteins*, **69**, 726–733.
27. Dominguez,C., Boelens,R. and Bonvin,A.M. (2003) HADDOCK: a protein-protein docking approach based on biochemical or biophysical information. *J. Am. Chem. Soc.*, **125**, 1731–1737.
28. Svergun,D.I., Barberato,C. and Koch,M.H.J. (1995) CRYSOL - a program to evaluate X-ray solution scattering of biological macromolecules from atomic coordinates. *J. Appl. Crystallogr.*, **28**, 768–773.
29. Theobald,D.L. and Wuttke,D.S. (2006) THESEUS: maximum likelihood superpositioning and analysis of macromolecular structures. *Bioinformatics*, **22**, 2171–2172.
30. Baker,N.A., Sept,D., Joseph,S., Holst,M.J. and McCammon,J.A. (2001) Electrostatics of nanosystems: application to microtubules and the ribosome. *Proc. Natl Acad. Sci. USA*, **98**, 10037–10041.
31. Dolinsky,T.J., Nielsen,J.E., McCammon,J.A. and Baker,N.A. (2004) PDB2PQR: an automated pipeline for the setup of Poisson-Boltzmann electrostatics calculations. *Nucleic Acids Res.*, **32**, W665–W667.
32. Lowman,H.B. and Draper,D.E. (1986) On the recognition of helical RNA by cobra venom V1 nuclease. *J. Biol. Chem.*, **261**, 5396–5403.
33. van Biesen,T., Soderbom,F., Wagner,E.G. and Frost,L.S. (1993) Structural and functional analyses of the FinP antisense RNA regulatory system of the F conjugative plasmid. *Mol. Microbiol.*, **10**, 35–43.
34. Meador,J. III, Cannon,B., Cannistraro,V.J. and Kennell,D. (1990) Purification and characterization of *Escherichia coli* RNase I. Comparisons with RNase M. *Eur. J. Biochem.*, **187**, 549–553.
35. Kurata,S., Ohtsuki,T., Suzuki,T. and Watanabe,K. (2003) Quick two-step RNA ligation employing periodate oxidation. *Nucleic Acids Res.*, **31**, e145.
36. Rambo,R.P. and Tainer,J.A. (2010) Bridging the solution divide: comprehensive structural analyses of dynamic RNA, DNA, and protein assemblies by small-angle X-ray scattering. *Curr. Opin. Struct. Biol.*, **20**, 128–137.
37. Tsutakawa,S.E., Hura,G.L., Frankel,K.A., Cooper,P.K. and Tainer,J.A. (2007) Structural analysis of flexible proteins in solution by small angle X-ray scattering combined with crystallography. *J. Struct. Biol.*, **158**, 214–223.
38. Dong,G., Chakshusmathi,G., Wolin,S.L. and Reinisch,K.M. (2004) Structure of the La motif: a winged helix domain mediates RNA binding via a conserved aromatic patch. *EMBO J.*, **23**, 1000–1007.

39. Ma,J.B., Ye,K. and Patel,D.J. (2004) Structural basis for overhang-specific small interfering RNA recognition by the PAZ domain. *Nature*, **429**, 318–322.
40. Stein,A.J., Fuchs,G., Fu,C., Wolin,S.L. and Reinisch,K.M. (2005) Structural insights into RNA quality control: the Ro autoantigen binds misfolded RNAs via its central cavity. *Cell*, **121**, 529–539.
41. Pontius,B.W. and Berg,P. (1990) Renaturation of complementary DNA strands mediated by purified mammalian heterogeneous nuclear ribonucleoprotein A1 protein: implications for a mechanism for rapid molecular assembly. *Proc. Natl Acad. Sci. USA*, **87**, 8403–8407.
42. De Guzman,R.N., Wu,Z.R., Stalling,C.C., Pappalardo,L., Borer,P.N. and Summers,M.F. (1998) Structure of the HIV-1 nucleocapsid protein bound to the SL3 psi-RNA recognition element. *Science*, **279**, 384–388.
43. Tompa,P. and Csermely,P. (2004) The role of structural disorder in the function of RNA and protein chaperones. *FASEB J.*, **18**, 1169–1175.
44. Gottesman,S. (2004) The small RNA regulators of *Escherichia coli*: roles and mechanisms. *Annu. Rev. Microbiol.*, **58**, 303–328.
45. Rajkowitsch,L. and Schroeder,R. (2007) Dissecting RNA chaperone activity. *RNA*, **13**, 2053–2060.
46. Kunte,H.J., Crane,R.A., Culham,D.E., Richmond,D. and Wood,J.M. (1999) Protein ProQ influences osmotic activation of compatible solute transporter ProP in *Escherichia coli* K-12. *J. Bacteriol.*, **181**, 1537–1543.
47. Milner,J.L. and Wood,J.M. (1989) Insertion proQ220::Tn5 alters regulation of proline porter II, a transporter of proline and glycine betaine in *Escherichia coli*. *J. Bacteriol.*, **171**, 947–951.
48. Smith,M.N., Crane,R.A., Keates,R.A. and Wood,J.M. (2004) Overexpression, purification, and characterization of ProQ, a posttranslational regulator for osmoregulatory transporter ProP of *Escherichia coli*. *Biochemistry*, **43**, 12979–12989.
49. Smith,M.N., Kwok,S.C., Hodges,R.S. and Wood,J.M. (2007) Structural and functional analysis of ProQ: an osmoregulatory protein of *Escherichia coli*. *Biochemistry*, **46**, 3084–3095.